



Highly efficient Cu-decorated iron oxide nanocatalyst for low pressure CO₂ conversion



Avik Halder^{a,1}, Martina Kilianová^{b,c,1}, Bing Yang^{a,1}, Eric C. Tyo^a, Soenke Seifert^d, Robert Prucek^{b,c}, Aleš Panáček^{b,c}, Petr Suchomel^{b,c}, Ondřej Tomanec^{b,c}, David J. Gosztola^e, David Milde^{b,f}, Hsien-Hau Wang^a, Libor Kvítek^{b,c,*}, Radek Zbořil^{b,c}, Stefan Vajda^{a,e,g,***}

^a Materials Science Division, Argonne National Laboratory, 9700 South Cass Avenue, Argonne, IL, 60439, United States

^b Regional Centre of Advanced Technologies and Materials, Faculty of Science, Palacký University Olomouc, Slechtitelu 27, CZ-78371, Olomouc, Czech Republic

^c Department of Physical Chemistry, Faculty of Science, Palacký University Olomouc, 17. listopadu 12, CZ-77146 Olomouc, Czech Republic

^d X-ray Science Division Argonne National Laboratory, 9700 South Cass Avenue, Argonne, IL, 60439, United States

^e Center for Nanoscale Materials, Argonne National Laboratory, 9700 South Cass Avenue, Argonne, IL, 60439, United States

^f Department of Analytical Chemistry, Faculty of Science, Palacký University Olomouc, 17. listopadu 12, CZ-77146 Olomouc, Czech Republic

^{*} Institute for Molecular Engineering, University of Chicago, Chicago, IL, 60637, United States

ARTICLE INFO

Keywords:

Iron oxide
Copper
Nanoparticles
Hydrogen
Carbon dioxide
Heterogeneous catalysis
CO₂ conversion
Carbon monoxide
Methane
Methanol
Benzene

ABSTRACT

We report a nanoparticulate iron oxide based catalyst for CO₂ conversion with high efficiency at low pressures and on the effect of the presence of copper on the catalyst's restructuring and its catalytic performance. *In situ* X-ray scattering reveals the restructuring of the catalyst at the nanometer scale. *In situ* X-ray absorption near edge structure (XANES) shows the evolution of the composition and oxidation state of the iron and copper components under reaction conditions along with the promotional effect of copper on the chemical transformation of the iron component. X-ray diffraction (XRD), XANES and Raman spectroscopy proved that the starting nanocatalyst is composed of iron oxides differing in chemical nature (α -Fe₂O₃, Fe₃O₄, FeO(OH)) and dimensionality, while the catalyst after CO₂ conversion was identified as a mixture of α -Fe, Fe₃C, and traces of Fe₅C₂. The significant increase of the rate CO₂ is turned over in the presence of copper nanoparticles indicates that Cu nanoparticles activate hydrogen, which after spilling over to the neighbouring iron sites, facilitate a more efficient conversion of carbon dioxide.

1. Introduction

Growing energy demands and environmental concerns have resulted in significant research interest for the conversion of CO₂. CO₂ hydrogenation using H₂ from sustainable sources is considered a promising method to help reduce CO₂ emissions by catalytically converting CO₂ into beneficial chemicals like alcohols (e.g. methanol), hydrocarbons (e.g. methane, benzene, etc.) or CO, with the subsequent opportunity for further processing. Although many endeavours have been invested to develop efficient processes for CO₂ conversion, significant improvements can be made by designing innovative catalysts. Moreover, gaining additional insights into CO₂ hydrogenation can aid in developing highly efficient catalyst and integrated process technology to meet the goals of mitigating greenhouse gas production and sustainable development of carbon market demands [1–6]. In essence,

methanol is produced in industry from syngas using mostly CuO/ZnO/Al₂O₃ catalyst [7]. However, many studies suggest that methanol can be directly formed from carbon dioxide [8–14]. Methanation of CO₂ or its transformation to CO especially on cheap catalysts, moreover on catalysts working under environmentally benign conditions, are other important routes of CO₂ conversion [6,15].

CO₂ conversion can progress via various routes, such as CO₂ hydrogenation to methane and other hydrocarbons, or to methanol. At higher reaction temperatures CO₂ conversion to carbon monoxide may become dominant as a result of the reverse water gas shift reaction (RWGS) [8,16–18]. The catalytic conversion of CO₂ was studied for example on iron-based catalysts as potential cost attractive candidates for CO₂ conversion into hydrocarbons or carbon monoxide [6,15,19,20]. It was also shown that iron-based catalysts with and without potassium promoter possess tunable selectivity and activity in

* Corresponding author at: Department of Physical Chemistry, Faculty of Science, Palacký University Olomouc, 17. listopadu 12, CZ-77146 Olomouc, Czech Republic.

** Corresponding author at: Materials Science Division, Argonne National Laboratory, 9700 South Cass Avenue, Argonne, IL, 60439, United States.

E-mail addresses: libor.kvitek@upol.cz (L. Kvítek), vajda@anl.gov (S. Vajda).

¹ A.H., M.K., and B.Y. equally contributing (first) authors.

CO₂ hydrogenation towards hydrocarbons at high pressures and CO formation at atmospheric pressure [21], and carbon nanotube-supported iron nanoparticles were found highly active in converting CO₂ to C_{1–5} products and CO [22]. In an attempt to control selectivity, iron-based catalysts enriched with gold particles or supported on oxides such as alumina, titania, zirconia, and zeolites were prepared and investigated as well [23–26].

There are many reports in the literature on various heterogeneous catalytic systems for the effective synthesis of methanol from CO₂. Copper-based catalysts prevail in these studies due to their high selectivity and less undesired by-products [6,20,27]. A vast number of support materials such as ZnO, ZrO₂, Al₂O₃, TiO₂, Fe₂O₃, ZnFe₂O₄, and SiO₂ have been tested for this purpose. In addition, multi-metallic materials with Cu as the main component were also studied [1,6,9,28–30]. Co-precipitation of metal salts with subsequent calcination has been the most widely used procedure to prepare the copper-based catalysts [31–36].

The present study focuses on the characterization and performance of a cost-efficient catalyst for the conversion of CO₂, based on iron oxide and copper, while considering the following. Iron oxide is commonly used for CO₂ or CO methanation/Fischer-Tropsch synthesis and can convert CO₂ into CO as well. Cu on the other hand is a highly efficient catalyst for CO₂ conversion to both CH₄ and CH₃OH [6,20,37,38]. Utilization of sonochemical method in synthesis of the nanocatalytic system can significantly improve its dispersity and therefore also catalytic activity [39,40].

The catalyst for this study was prepared as a nanostructured iron oxide decorated with copper nanoparticles. The synthesis of the catalysts was carried out using a novel sonication reduction method. The evolution of the as-prepared catalysts was monitored under reaction conditions using a combination of *in situ* X-ray scattering and X-ray absorption techniques, the catalytic performance using temperature-programmed reaction. Additional characterization of the catalyst before and after reaction was performed by Raman spectroscopy, XRD, scanning transmission electron microscopy (STEM), and high resolution transmission electron microscopy (HRTEM) including scanning transmission electron microscopy (STEM) and energy dispersive spectrometry (EDS).

2. Experimental

2.1. Synthesis of FeNC and Cu-FeNC nanocomposite catalysts

Synthesis of the iron oxide catalyst supporting material was performed using the following two-step procedure. Briefly, the synthesis protocol starts with direct precipitation of iron(II) oxalate precursor from an equimolar mixture of oxalic acid ($\geq 99\%$, Aldrich) and Fe(II) chloride (98%, Aldrich) in N,N-dimethylacetamide (anhydrous, 99.8%, Sigma-Aldrich) at room temperature followed by the solid-state isothermal treatment at 175 °C for 12 h in air [41,42]. Copper was added using a sonication technique as follows. Typically, 200 mg of already-prepared iron oxide nanoparticles were dispersed in 188 mL of distilled water. Next, 2 mL of 15.7 mmol/L aqueous copper sulfate pentahydrate solution ($\geq 99\%$, Sigma), recalculated to final concentration of 1 wt% of Cu, was added to the mixture and the pH of the dispersion was adjusted to 10 using 1 M sodium hydroxide ($\geq 97\%$, Fluka). Hydrazine hydrate (reagent grade, Sigma-Aldrich) was utilized as a moderately strong reducing agent. Sonication of the dispersion was performed using a Qsonica (Q700 with Ti horn part 4418) for 10 min under intensity equal to 25.37 kJ. After several seconds of sonication that brought full dispersion of the iron oxide in the entire volume, 10 mL of 4.95 mmol/L solution of hydrazine hydrate was added into the reaction system. After 10-min sonication, the nanocomposite of iron oxide with 1 wt% of Cu (denoted as Cu-FeNC) was separated by centrifugation and washed two times with distilled water. The washed and separated nanocomposite was dried in a flowbox with nitrogen as an inert purging

gas. A reference sample (denoted as FeNC or FeNC blank), was prepared using the same procedure excluding the addition of copper sulfate solution which was replaced by distilled water. The sonochemical method of nanocatalyst preparation has a significant benefit over conventional co-precipitation method as it offers the possibility to prepare copper nanoparticles exclusively on the surface of the support [39,40].

For the characterization and reactivity experiments, the Cu-FeNC and the corresponding FeNC blank were drop-casted on oxidized silicon wafers (SiO₂/Si(100)).

2.2. *In-situ* grazing incidence small-angle X-ray scattering (GISAXS) and X-ray absorption near edge spectroscopy (GIXANES)

A special system designed for simultaneous *in-situ* GISAXS and GIXANES was utilized to characterize the FeNC blank and Cu-FeNC samples under reaction conditions [43–45].

The *in-situ* experiments were performed by placing the samples on a ceramic heater in a custom built reaction cell [46]. The temperature of the sample was measured with a K-type thermocouple inserted into the middle of the heater. The thermocouple was attached to a temperature controller (Lakeshore model 340) which controlled the output of a KEPCO power supply (model ATE 55–5DM). The experiment was performed by applying two consecutive identical temperature ramps between 25 °C and 375 °C as shown in Fig. S1. The total measurement took 24 h. Prior to the start of the temperature ramp, the reaction cell and gas lines were evacuated to about 0.02 atm and flushed with pure He three times before the introduction of the reaction gas mixture. A gas-mixing unit consisting of calibrated mass flow controllers (Brooks model SLA5850) was used to control the gas composition and its flow rate into the reaction cell: 1% carbon dioxide and 3% hydrogen in He at a flow rate of 20 sccm and 1.25 atm pressure (*i.e.* 0.0125 atm and 0.0375 atm partial pressure of CO₂ and H₂). Within the individual ramps, the temperature was increased in 50 °C increments at a heating rate of 10 °C per minute between the temperature steps and dwelling 30 min at each temperature. At each temperature, GISAXS and GIXANES data were collected.

The *in-situ* reaction cell was fitted with Kapton windows to facilitate X-ray transmission. The cell was fixed on a computer controlled goniometer to adjust angle and position of the sample for grazing incidence geometry. The X-ray beam was scattered off the sample surface near the critical angle ($\alpha_c = 0.18$ at Cu K-edge and $\alpha_c = 0.2$ at Fe K-edge) of the Si substrate. The GISAXS experiments were performed with X-rays of 8.993 keV and 7.112 keV for Cu-FeNC and FeNC respectively. A 1024 × 1024 pixel two-dimensional CCD detector (Platinum) was used for recording the two dimensional GISAXS images from the samples. The collected data were analyzed by Moore autocorrelation [47]. GIXANES spectra on Cu K-edge and Fe K-edge were collected using a 4-element germanium fluorescence detector (Vortex) arranged perpendicularly to the X-ray beam and parallel to the sample surface. The GIXANES data were analyzed using the ATHENA and MATLAB software packages [46,48,49].

2.3. Temperature-programmed reactivity

The catalytic activity of the samples was measured separately in the laboratory using an identical set-up as used at the synchrotron and under identical reaction conditions (25 °C to 375 °C, with 20 sccm flow of 1% CO₂ and 3% H₂ gas mixture carried in helium at pressure of 1.25 atm, the cell volume was ~ 20 cm³ resulting in a gas hourly space velocity (GHSV) of 60 h⁻¹) and using the same temperature ramp as at the synchrotron. The reaction products were monitored on a quadrupole mass spectrometer (Pfeiffer Prisma QMS 220) sampling with an electronic gas regulating valve (EVR 116, Pfeiffer) on the inlet of the mass spectrometer set to 5×10^{-6} mbar pressure in the mass spectrometer. Before the start of the temperature ramp, the reaction gas mixture was flown continuously for about 10 h to minimize and

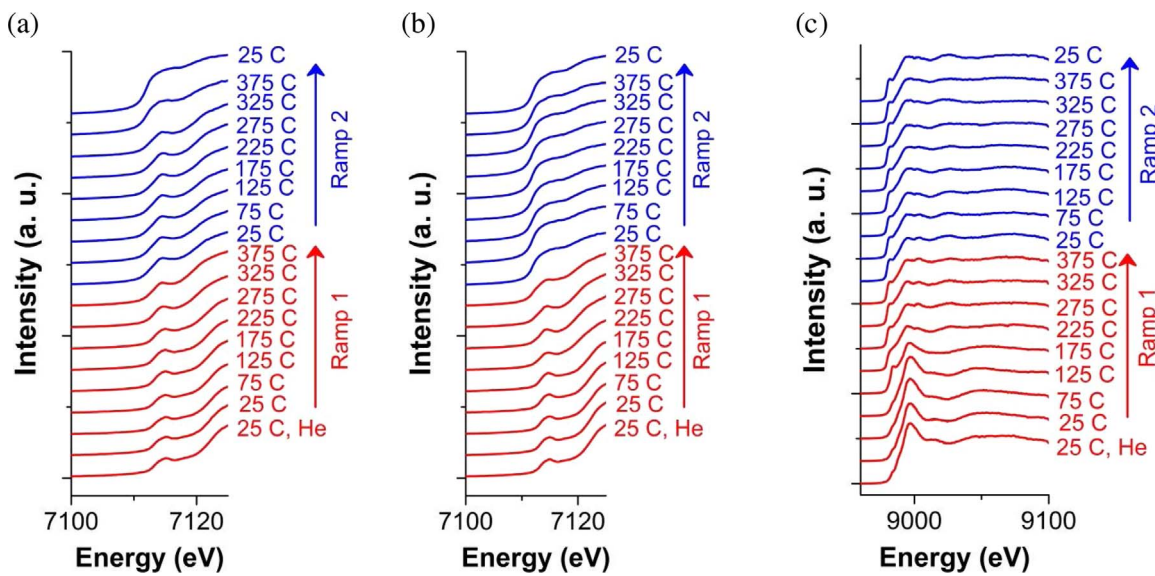


Fig. 1. *in situ* XANES spectra (pre-edge region) collected for FeNC sample (a) and for Cu-FeNC sample (b) at Fe K-edge. For XANES collected at the Fe K-edge, the pre-edge region is plotted which shows distinctive features from different composition. XANES spectra of Cu-FeNC sample at Cu K-edge (c). The lower part of curves from 25 to 375 °C (red lines in web version of the article) correspond to the first ramp, and the upper part of curves from 25 to 375 °C (blue lines in web version of the article) to the second ramp.

stabilize the background signal of the mass spectrometer. Certified analytical grade gases were mixed with helium (Air Gas Inc.) to calibrate the mass spectrometer.

2.4. Ex-situ characterization of the nanocomposite catalysts

HRTEM images were primarily obtained using a JEM2010 microscope operated at 160 keV with a point-to-point resolution of 1.9 Å. Detailed HRTEM investigations were performed at 80 kV accelerating voltage on an FEI Titan G2 60–300 transmission electron microscope equipped with an X-FEG electron gun, a STEM high-angle annular dark-field detector (HAADF) and a chemiSTEM EDS detector. Additionally, field emission scanning electron microscope (FESEM) images were taken on a Hitachi 6600 FEG microscope operating in the secondary electron mode and using an accelerating voltage of 5 kV.

The determination of copper ($m/z = 63$) and iron ($m/z = 56$) quantities in the samples was performed by ICP-MS (Agilent 7700x, Japan) equipped with quadrupole mass analyzer and octupole reaction system working in helium mode for interference reduction. The concentration of Cu was quantified against an external calibration curve prepared from aqueous calibration solution with certified concentration of Cu and Fe at 1.000 ± 0.002 g/L (Analytika spol. s r.o., Czech Republic). For the present experiments we used 2.6 mg of FeNC and 2.5 mg of Cu-FeNC catalyst. The content of Cu in Cu-FeNC sample was determined at level of 9.85 mg/g (calculated concentration in the preparation procedure was 1% w/w = 10 mg/g) while no Cu was detected in the FeNC catalyst. The determined content of Fe in the Cu-FeNC and FeNC catalyst samples were 421.97 mg/g and 494.69 mg/g respectively. The absolute loadings of Cu and Fe in the two catalysts are as follows: (i) FeNC sample contained 1.245 mg of Fe and no detectable amount of Cu, (ii) Cu-FeNC sample contained 1.073 mg of Fe and 0.025 mg of Cu. We also estimated the number of Cu sites on the surface of iron oxide support in Cu-FeNC catalyst. Taking into consideration the total amount of the Cu loading and the average size of the Cu nanoparticles as ~5 nm, we estimated $\sim 2 \times 10^{13}$ nanoparticles of Cu on the surface of iron oxide support. This value was computed for 2.5 mg of catalyst used in the study. This also corresponds to the presence of a total number of 4×10^{16} Cu nanoparticles per m^2 of catalyst surface.

Raman spectra were recorded using a Raman microscope (inVia Reflex, Renishaw, Inc.) using 514 nm excitation from an argon ion laser. The samples were excited and the scattered light was collected

though a 20x objective (Leica, NA = 0.40). The mapped area covered a $33 \times 19.5 \mu\text{m}$ area and spectra were collected at $1.5 \mu\text{m}$ increments. Each spectrum consisted of 30 s averaged integrations with 0.12 mW incident laser power.

X-ray powder diffraction (XRD) patterns of investigated samples were obtained by using a Miniflex diffractometer in Bragg–Brentano geometry (Rigaku Corp.) equipped with an iron-filtered Cu K α radiation source ($\lambda = 0.154 \text{ nm}$) at typical running conditions: Cu/30 KV/15 mA, K β filter, scattering slit 4.2 deg, receiving slit 0.3 mm and at Fixed time (FT) Scan mode. The acquired patterns were processed using X'Pert HighScore Plus software (PANalytical, The Netherlands), in combination with PDF-4+ and ICSD databases.

The specific surface area of the prepared catalysts was determined from adsorption-desorption isotherms which were measured at a temperature of 77.4 K up to its saturation pressure (Brunauer, Emmett, Teller, BET). Isotherms were acquired by the statistic volumetric technique on Autosorb IQ (Quantachrome) instrument, yielding $199 \text{ m}^2/\text{g}$ for both types of catalysts.

3. Results and discussion

3.1. In-situ characterization of FeNC and Cu-FeNC catalysts

3.1.1. X-Ray absorption near edge spectroscopy (XANES)

In-situ XANES in grazing incidence mode (GIXANES) was utilized to characterize the FeNC blank and Cu-FeNC samples, the copper component at the Cu K-edge (8.979 keV) and iron component at the Fe K-edge (7.112 keV) during the temperature ramps are shown in Fig. 1.

XANES spectra collected at the Fe K-edge for both FeNC (Fig. 1a) and Cu-FeNC (Fig. 1b), at 25 °C under He and reactant gases resemble a mixed phase of $\alpha\text{-Fe}_2\text{O}_3$, FeO(OH), and trace amount of Fe_3O_4 and metallic Fe with an average oxidation state of ~2.8 as seen from Fig. 2a–d. The Fe pre-edge region within the energy range 7.1 and 7.12 keV is chosen to monitor the evolution of the iron component, for its distinctive features changing with the composition and oxidation state of iron [50,51].

Notable differences appear at higher temperatures for the two catalysts at 225 °C, at which iron in FeNC starts reducing, with the content of Fe_3O_4 and metallic Fe rising (Fig. 2a–b). At the end of the first heating ramp FeNC consists of about 15% metallic Fe. A slight increase in the average oxidation state of the FeNC sample is seen between 25 °C

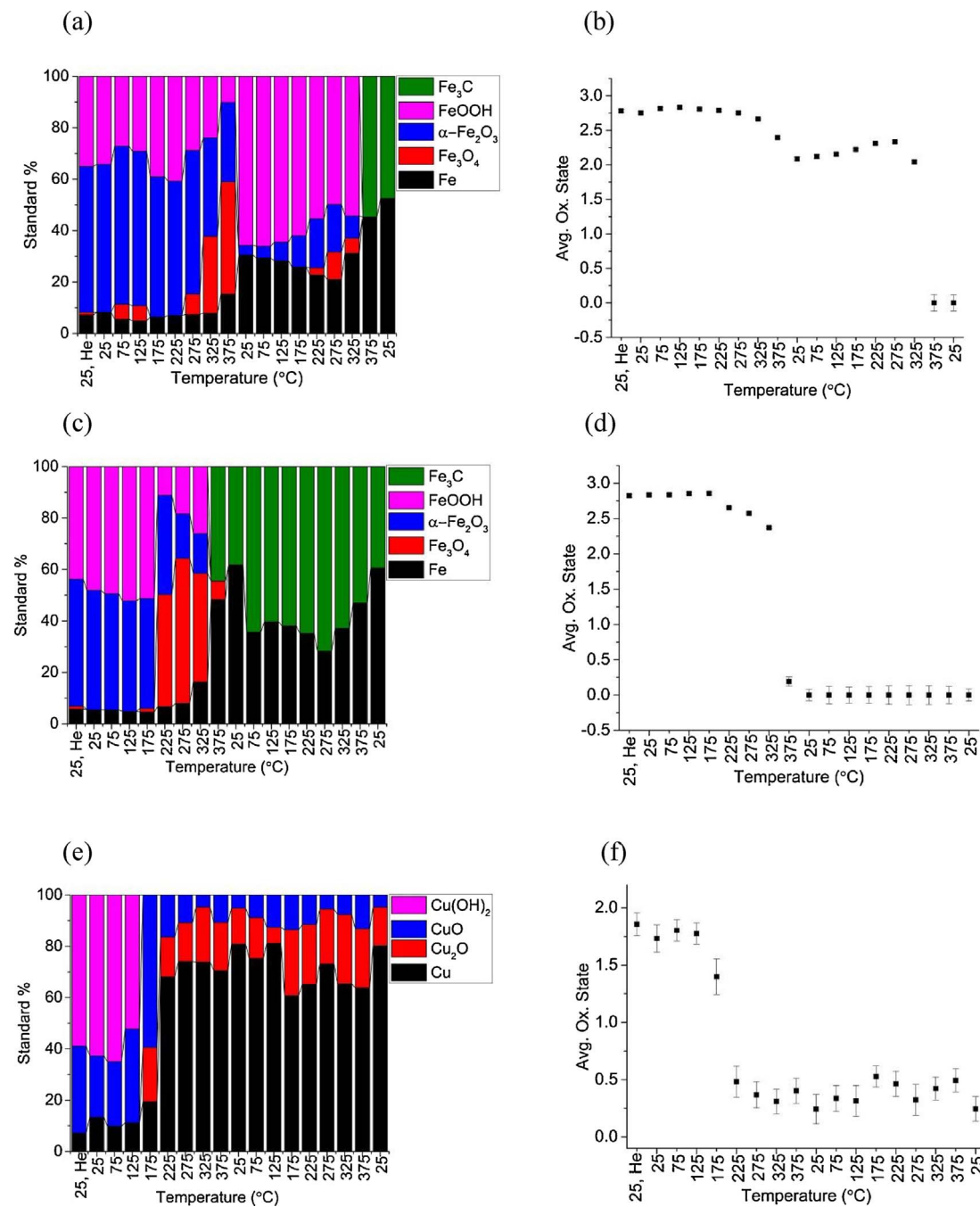


Fig. 2. Linear combination fit results of Fe K-edge XANES spectra (a) and average oxidation state of Fe for the FeNC sample (b). Linear combination fit results of Fe K-edge XANES spectra (c) and average oxidation state of Fe for the Cu-FeNC sample (d). Linear combination fit results of Cu K-edge XANES spectra (e) and average oxidation state of Cu for the Cu-FeNC sample (e). Linear combination fits (see example at Fig. S2) were based on the spectra of bulk standards (Fig. S3).

and 275 °C during second ramp which likely reflect the complex evolution of the multicomponent oxide/hydroxide phase before the transition to the final iron/iron-carbide composition. Full reduction to a mixed Fe and Fe₃C phase occurs at 375 °C in the second ramp. The reduction of iron in Cu-FeNC (Fig. 2c-d) starts in a similar way at 225 °C, when the content of Fe₃O₄ and metallic Fe starts to rise.

Thereafter, iron continues to gradually reduce to an average oxidation state of ~2.2 at 325 °C, after which a sharp reduction to oxidation states 0 occurs at 375 °C, revealing a mixture of metallic iron and iron carbide. This is a strong indication of copper promoted reduction of iron, likely caused by the presence of Cu nanoparticles which can activate hydrogen spilling over to the neighbouring iron oxide sites that facilitates the reduction (see below for the reduction of Cu)[52]. After

the first ramp only slight changes occurred in the composition or oxidation state of the iron component of Cu-FeNC.

The analysis of the Cu K-edge XANES spectra collected on Cu-FeNC at 25 °C under He and reactive gas mixture reveal an average oxidation state of ~1.8 for Cu and a mixed phase of CuO and Cu(OH)₂ (see Fig. 2e-f). The first significant change is recorded at 175 °C during the first ramp, where the fraction of Cu₂O and metallic Cu components rapidly increased at the expense of the CuO and Cu(OH)₂ components, with the average oxidation state of copper dropping to ~1.4. Above 225 °C of the first heating ramp and during the entire second ramp Cu is found in an average oxidation state between ~0.2 and 0.5, with a dominant fraction of metallic Cu, and a small fraction (~20–25%) of Cu₂O and CuO components. The results show that in Cu-FeNC the

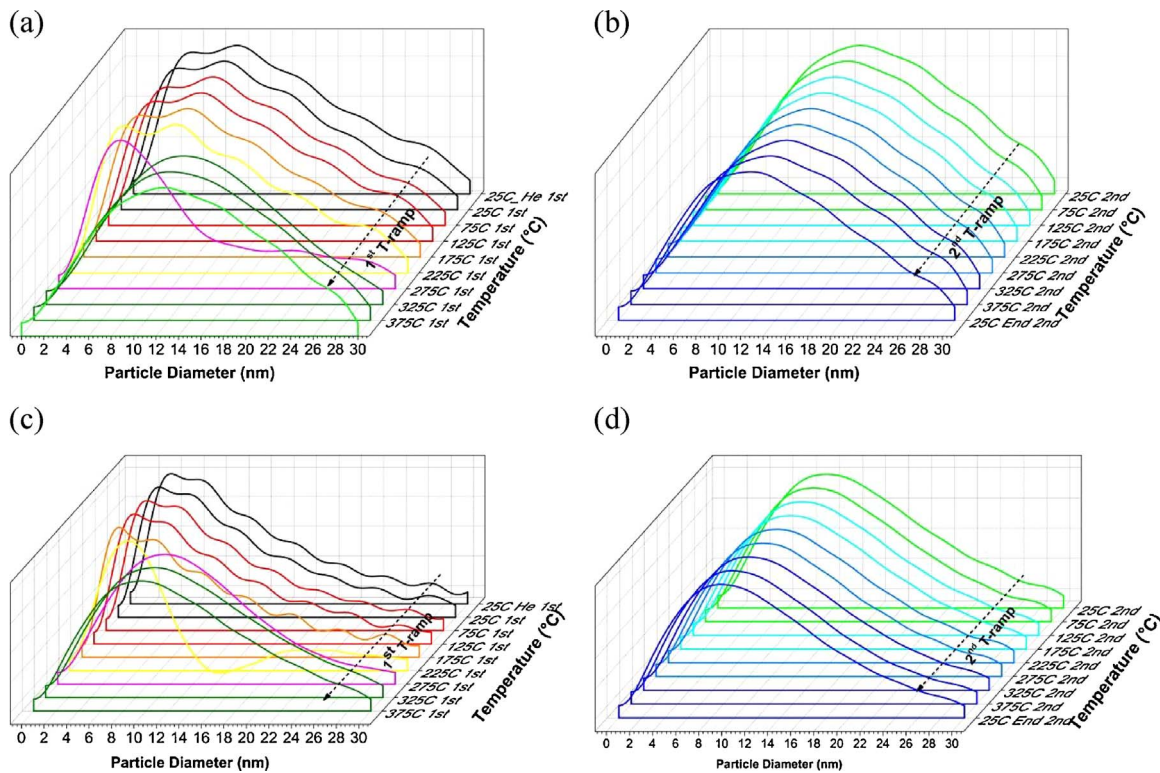


Fig. 3. GISAXS data analysis for FeNC and Cu-FeNC samples. Evolution of the size distribution of the nanoscale components of the FeNC sample during first ramp (a) and second ramp (b). The evolution for Cu-FeNC sample for first and second ramp are shown in (c) and (d) respectively.

reduction of the iron component in the catalysts is preceded by the reduction of its copper component from which hydrogen spill-over may occur [53], promoting the reduction of the iron component of the catalysts.

3.1.2. Grazing incidence small angle X-ray scattering (GISAXS)

In parallel with *in-situ* XANES, GISAXS data were collected to monitor the evolution of the size distribution of the nanoscale components in the FeNC blank and Cu-FeNC catalysts under reaction conditions. Cuts of the GISAXS images shown in Fig. 3 reveal that the nanometer-sized components of the catalysts evolve differently during the first ramp, after which they stabilize.

GISAXS data for the FeNC blank were collected at the Fe K-edge at 7.112 keV. A wide multimodal distribution of the particle size is found in the as-made sample, with a main peak around 10 nm and smallest particle size of about 5 nm (see Fig. 3a). The wide size distribution reflects the presence of different nanoparticulate sizes, structures and morphologies seen also by microscopies (shown below). The size distribution remains unchanged up to 275 °C during the first ramp. The first change is observed at 275 °C during the first ramp, with a main peak at ~5 nm. At 325 °C, the size distribution evolves into a broad continuous distribution with a peak between ~11–12 nm which remains unchanged during the second ramp as we show in Fig. 3(b).

For Cu-FeNC, GISAXS data collected at the Cu K-edge (8.993 keV) are shown in Fig. 3c. In comparison with the GISAXS data obtained for the FeNC blank, an additional peak at ~3 nm is observed for Cu-FeNC, which can be attributed to the Cu nanoparticles observed in the as-made Cu-FeNC seen by TEM as shown below. The first change is observed at 225 °C during the first ramp, with a main peak at ~5 nm. The size distribution of the nanoscale components undergoes significant change at 275 °C of the first ramp, converging to a broad unimodal particle size distribution with a peak around 9–10 nm. No further change in the size distribution occurred with temperature increment, or during the second ramp (Fig. 3d) of the reaction cycle. Thus, copper does not seem to have a significant effect on the resulting size of the

nanometer sized iron structures of the catalyst. Surprisingly, the peak at ~3 nm assigned to copper nanoparticles disappears during the temperature ramp. Based on the HRTEM of the spent Cu-FeNC, this may be caused by the growth of the Cu particles and/or their partial embedment into the support FeNC. The growth of the particles is most likely caused by thermal annealing, because it takes place at a similar temperature during the first ramp for both FeNC and Cu-FeNC catalysts.

3.2. Ex-situ characterization of the FeNC and Cu-FeNC catalysts

3.2.1. Electron microscopy and EDS elemental mapping

The as-made (“fresh”) and spent samples were characterized using FESEM, TEM, HRTEM, and HAADF-STEM. FESEM images of the FeNC and Cu-FeNC sample before and after catalytic reaction are shown in Fig. 4, showing the presence of various morphologies. Additional FESEM images are shown in Fig. S4. The image collected on the as-made catalyst shows the presence of morphologies that can be attributed to certain Fe compounds. The rod- and plate-like structures represent metallic Fe (Fig. 4a, c, and Fig. S4a, c) [54,55], the flowers indicate the presence of α -Fe₂O₃, the nano-husks represent α -FeO(OH) (Fig. 4a, c and S4e) [56], and traces of grains are typical of Fe₃O₄ (Fig. 4a, c) [57]. Highly magnified images of the nanorods and scales are shown in Fig. 4e, f with a smooth and structured surface of the fresh and spent catalysts. The surface of the spent catalysts develops intertwined polymorphs (Fig. 4b, d, f) which is indicative of the presence of Fe₃C [56,58–61]. TEM images collected from fresh Cu-FeNC samples shown in Fig. S5 further confirm the presence of plate-like structures from metallic Fe, husk-/rod-like FeO(OH), and globular structures from the iron oxide phases like α -Fe₂O₃ and Fe₃O₄.

HRTEM of the as made and spent FeNC shows the presence of ~5–8 nm and ~10–20 nm sized nanoscale particles of Fe species (Fig. 5a, b), in good agreement with the findings from GISAXS. The image collected on the fresh and spent Cu-FeNC shows the presence of Cu nanoparticles of sizes within ~2–4 nm and ~5–7 nm, respectively as shown in Fig. 5c, d. In the spent Cu-FeNC, the Cu particles seem to be

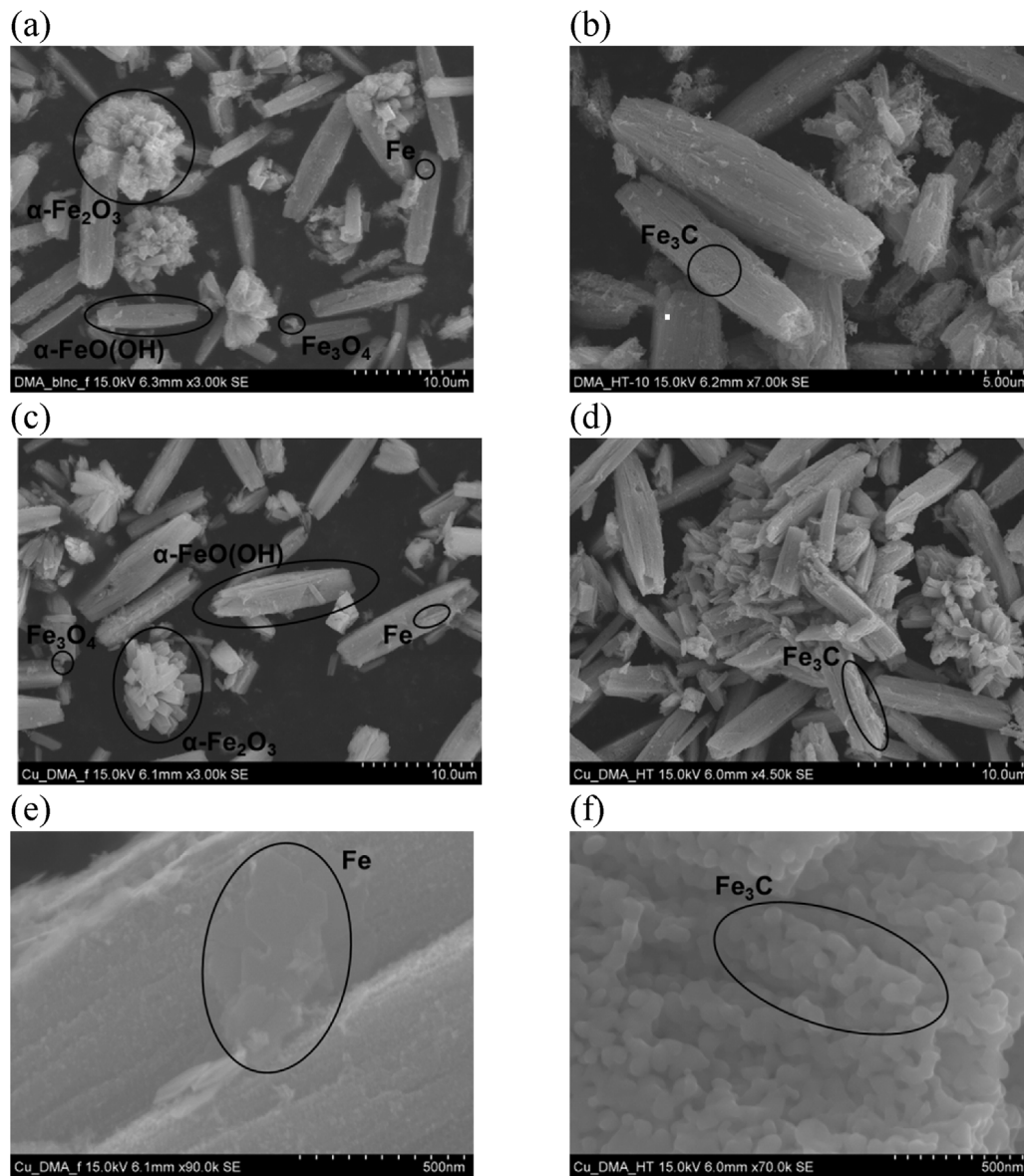


Fig. 4. FESEM images of fresh and spent FeNC and Cu-FeNC samples: fresh FeNC (a), spent FeNC (b), fresh Cu-FeNC (c), spent Cu-FeNC (d), flakes/plates on the smooth surface of fresh Cu-FeNC (e), surface intertwined with polymorphs on spent Cu-FeNC (f). The dominating phases for each sample are marked within the micrographs.

partially embedded into FeNC. HAADF-EDS mapping of the fresh (Fig. 6) and spent Cu-FeNC (Fig. S6) shows uniform distribution of copper. An iron oxide layer forming a thin shell on the surface of metallic iron is clearly visible for the Cu-FeNC catalyst (Fig. S6). The oxide layer forms on the surface of metallic iron (which is the dominant phase at the end of the reaction) as the catalysts are exposed to air after the reaction.

3.2.2. Raman and XRD characterization

Raman spectra were collected on the FeNC and Cu-FeNC samples before and after reaction. Both fresh catalysts showed a combination of the following iron oxide phases: α -Fe₂O₃ (hematite), α -FeO(OH) (goethite) and a trace amount of Fe₃O₄ (magnetite) (see Fig. S7a, c [61–68]). The presence of iron oxide and oxyhydroxide phases could also be seen under XANES shown in Fig. 1 and 2. In the spent samples, the Raman bands related to α -FeO(OH) (241 cm⁻¹) and Fe₃O₄ (677 cm⁻¹) disappeared and a broad peak appeared around 1600 cm⁻¹, assigned to Fe₃C formed [69]. The appearance of broad band around 1300 and 1600 cm⁻¹ may be indicative of the formation of graphitic or other form of carbon during the reaction as well. The disappearance (or weakening) of multiple oxide and oxyhydroxide peaks present in the fresh sample is an additional evidence for the

reduction of the iron oxide [66] as witnessed by *in situ* XANES discussed above. The appearance of the hematite band on the spent catalysts is caused by the oxidation of the surface of the catalyst during exposure of the samples to air between the *in situ* experiment and recording the Raman spectra. Since Raman is a surface sensitive technique the presence of the oxides dominates in the spectra. Thus, once the catalyst is exposed to air it needs to be reactivated.

XRD of the fresh FeNC and Cu-FeNC sample shows diffraction peaks that can be assigned to α -Fe₂O₃, FeO(OH), and Fe₃O₄ (see Fig. S7b, d [60,70]). In the spent samples, sharp peaks appear which can be assigned to a mixture of Fe₃C and metallic Fe nanocomposite [71]. The presence of trace amount of Fe₅C₂ is also possible [72], but cannot be clearly distinguished due to its overlap with the dominating Fe₃C peaks. These results are consistent with the observations made by *in situ* XANES. An additional strong peak at $\sim 42.5^\circ$ occurs in the spent Cu-FeNC due to Cu nanoparticles [73] grown into the detectable range of XRD (c.f. ~ 5 –6 nm sized Cu particles from HRTEM).

3.3. Reactivity measurement on FeNC and Cu-FeNC

To study the catalytic activity of the FeNC blank and the Cu-FeNC nanocomposite, we followed the production of expected main products

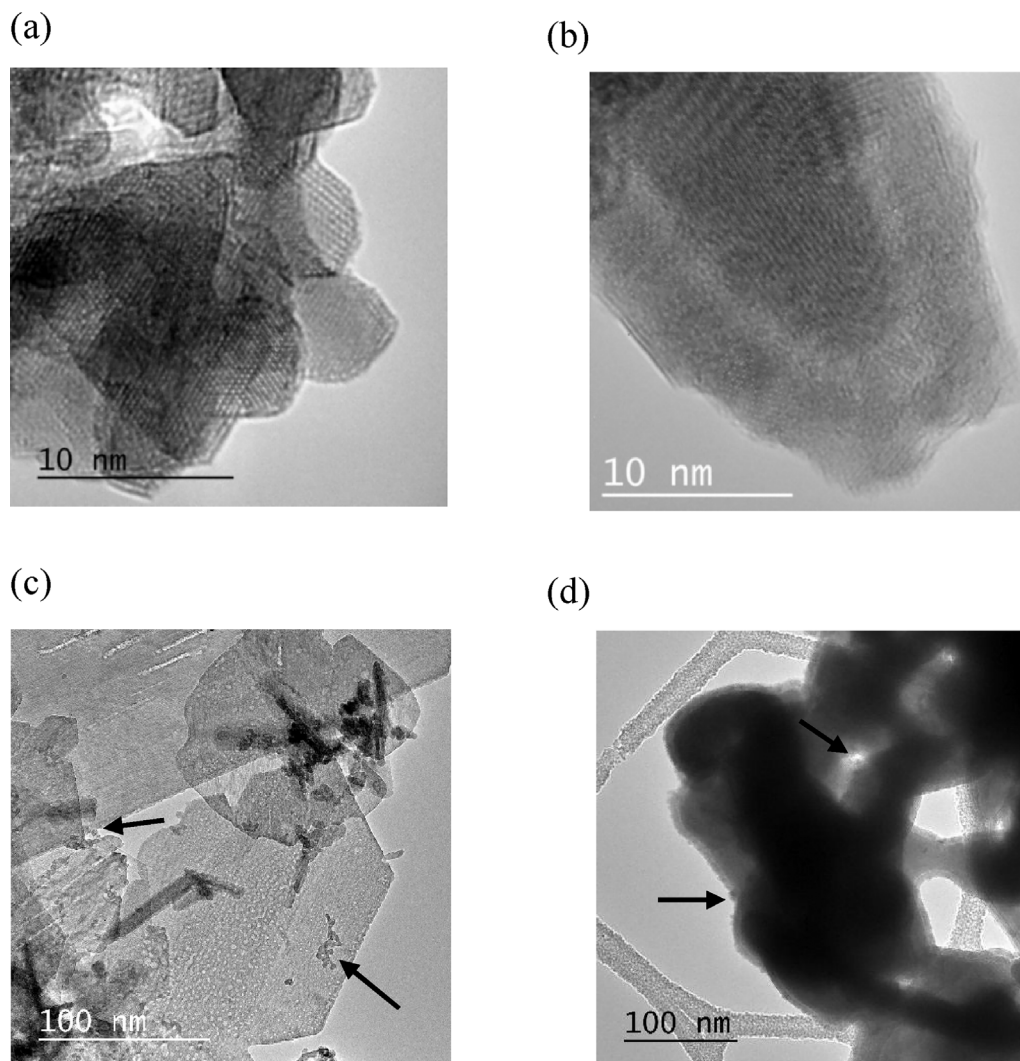


Fig. 5. HRTEM images collected on fresh FeNC (a), spent FeNC (b), fresh Cu-FeNC (c), and spent Cu-FeNC (d). The arrows on figures with Cu-FeNC catalysts (fresh and spent) point to Cu nanoparticles on the surface of the Fe support.

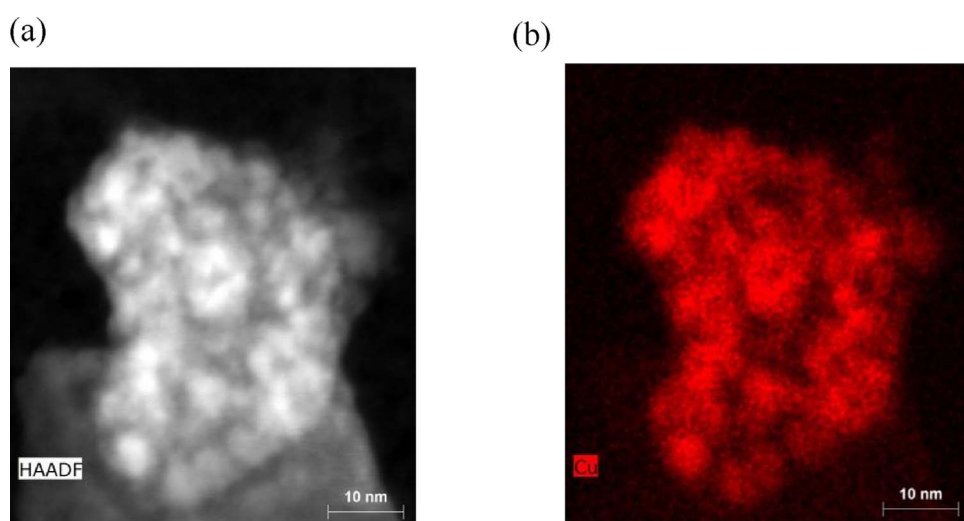


Fig. 6. HAADF/EDS chemical mapping of the fresh Cu-FeNC sample showing homogeneous distribution of Cu species over Fe-O based nanostructures. HAADF image (a), and Cu chemical map (b), confirming the presence of small Cu nanoparticles.

such as carbon monoxide, methane, methanol, and benzene [74,75], using temperature programmed reaction (TPRx) by monitoring selected mass/fragment signals (m/z) with a mass spectrometer. We note that during the first heating ramp, the catalysts evolved in their oxidation state and morphology as described in the XANES and GISAXS sections. Consequently, the following section will focus on the activity data

collected during the second heating ramp. The raw signals of the products as collected are shown in Fig. S8 and the carbon based selectivity is plotted in Fig. S9. Because both studied catalytic systems are based on Fe support, the activity of the catalysts was primarily evaluated as per Fe atom turn-over rate (TOR) – the number of CO_2 molecules consumed and the number product molecules produced per total Fe atom of

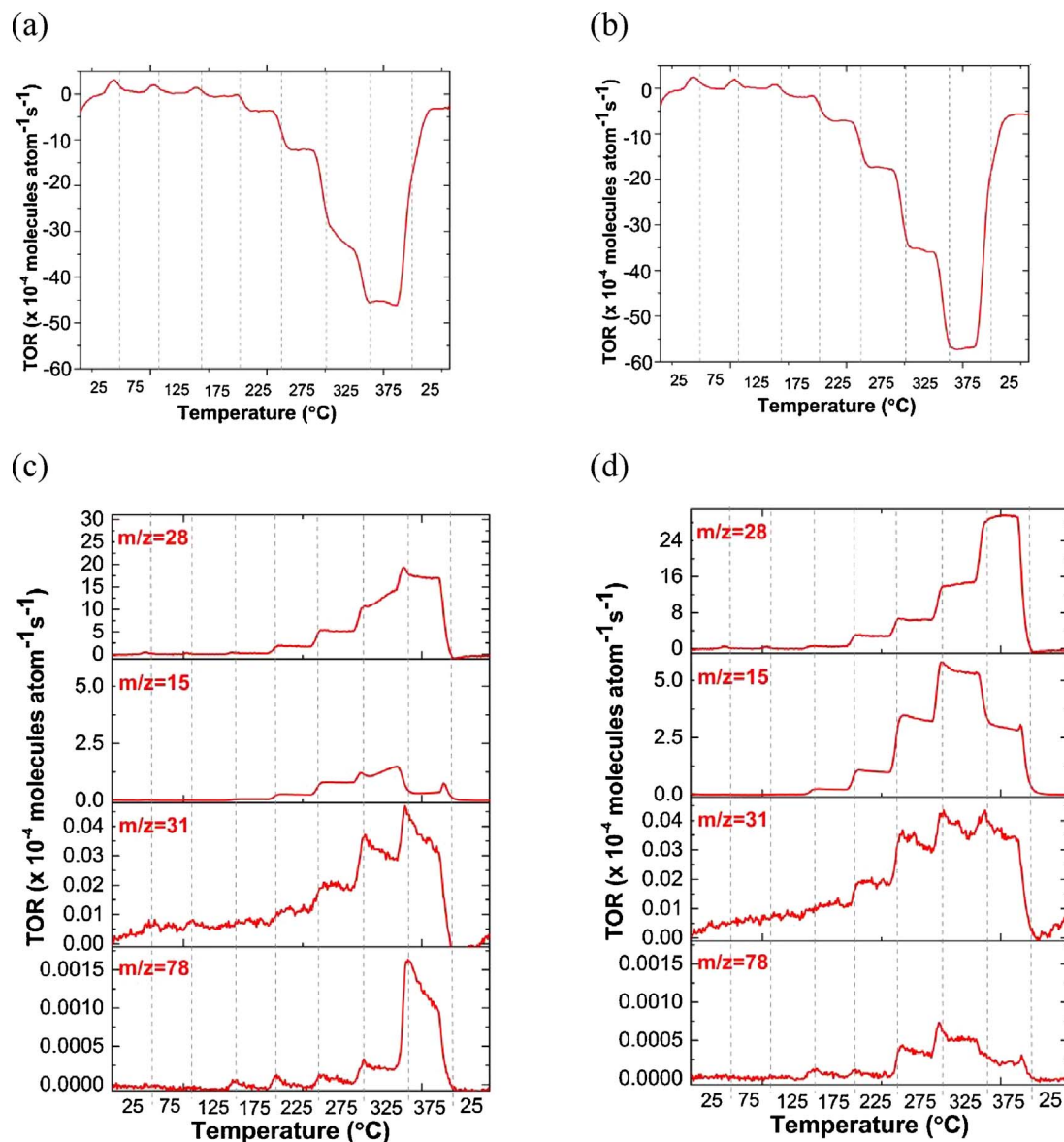


Fig. 7. Temperature dependence of TORs per total Fe atom during the second ramp for CO_2 ($m/z = 44$) for (a) FeNC, and (b) Cu-FeNC. In (c) and (d) the TOR for CO ($m/z = 28$), methane ($m/z = 15$), methanol ($m/z = 31$), and benzene ($m/z = 78$) are presented for FeNC and Cu-FeNC respectively. Temperature-dependent selectivity plots are shown in Fig. S9.

the sample per second, as shown in Fig. 7 for the second ramp (see Fig. S1 for the double temperature ramp applied). The CO_2 turnover rate reaches a value of $\sim 4.5 \cdot 10^{-3}$ molecules atom $^{-1}\text{s}^{-1}$ and $5.7 \cdot 10^{-3}$ molecules atom $^{-1}\text{s}^{-1}$ for FeNC (Fig. 7a) and Cu-FeNC (Fig. 7b) respectively, which is significantly higher compared to other known catalysts [15,72]. The TOR of CO_2 is found to be $\sim 35\%$ higher for Cu-FeNC compared to the FeNC catalyst.

As far as catalyst stability/evolution is considered, in the case of Cu-FeNC one could see from the XANES analysis (Figs. 1 and 2) that the composition does not change after the first cycle at either Cu K-edge or the Fe-K-edge. This indicates that both the Cu nanoparticles and the iron mixture reach their final state in the first cycle. Additional evidence is provided by the stable CO_2 signal at each temperature step. In case of FeNC the composition of the catalyst reaches its final state at the end the second ramp.

3.3.1. Methane and CO formation

Cu-FeNC turned out as to the best our knowledge one of the most active catalysts for methanation of CO_2 , with a TOR of 5.4×10^{-4} molecules atom $^{-1}\text{s}^{-1}$ (STY 236 g kg $^{-1}\text{h}^{-1}$) at 325 $^{\circ}\text{C}$, as shown in

Fig. 7d. For comparison, La_2O_3 activated Ni based catalyst has a TOR of 3×10^{-4} molecules atom $^{-1}\text{s}^{-1}$ (STY 1180 g kg $^{-1}\text{h}^{-1}$) at 380 $^{\circ}\text{C}$ and 12 atm [6]. At 375 $^{\circ}\text{C}$ the methanation activity drops on Cu-FeNC by 50% (STY 120 g kg $^{-1}\text{h}^{-1}$), and CO production increases to 3×10^{-3} molecules atom $^{-1}\text{s}^{-1}$ (STY 2280 g kg $^{-1}\text{h}^{-1}$). It should be mentioned that STY for Cu-FeNC catalyst was computed based on weight of the fresh catalyst. If the changes in chemical nature of the catalyst observed via XANES will be taken in to account (iron oxides are transformed to the zero-valent iron and Fe_3C in the ratio 1:1 at 375 $^{\circ}\text{C}$), the value of STY for CH_4 production should increase in this case up to a value of about 500 g kg $^{-1}\text{h}^{-1}$.

These trends are consistent with previously published studies which revealed that higher reaction temperatures in CO_2 hydrogenation favor both methanation reaction and RWGS reaction to produce methane and carbon monoxide, respectively due to thermodynamic limitation of reaction pathway for methanol production [18,24,32,36]. At 325 $^{\circ}\text{C}$ the activity of FeNC towards methane was $\sim 30\%$ of the one obtained on Cu-FeNC and dropped significantly at 375 $^{\circ}\text{C}$ at which the CO formation activity of FeNC peaked at 375 $^{\circ}\text{C}$ at $\sim 70\%$ relative to CO formed on Cu-FeNC at 375 $^{\circ}\text{C}$ (see Fig. 7c and d), thus showing

different selectivity of the two catalysts towards methane and CO. The per total Fe atom CO activity obtained under low pressure compares favourably with the reported value of 0.12 molecules (surface Cu atom) $^{-1}$ s $^{-1}$ measured on polycrystalline Cu foil at 5 bar pressure and 237 °C [76]. The formed CO can then be further converted to long chain hydrocarbons by tandem catalysis, using suitably designed Fischer-Tropsch catalysts like Co, including under low pressure [77]. Alternatively CO can be removed by adsorption and further processing on a catalyst surface like Pt, Rh [78], or carbon supported Pd catalyst [79].

3.3.2. Methanol formation

The catalytic performance of the FeNC and Cu-FeNC catalysts were found to be significantly different. FeNC produced $\sim 4 \cdot 10^{-6}$ molecules atom $^{-1}$ s $^{-1}$ (3.5 g kg $^{-1}$ h $^{-1}$) of methanol at 375 °C, while Cu-FeNC reached this value at much lower temperature of 275 °C (see Fig. 7c and d). Moreover, Cu-FeNC was much more active at lower temperatures than FeNC and exhibited measurable activity already at 175 °C in comparison with FeNC's at 225 °C. The observed TOR compares acceptably well with other bulk catalysts, measured at similar temperature but at much higher pressure. (For comparison see the to our knowledge best reported Cu/ZnO/ZrO₂ based catalyst having a TOR of $9 \cdot 10^{-5}$ molecules atom $^{-1}$ s $^{-1}$ at 5 MPa [20]. In our experiment the partial pressure of CO₂ and H₂ was 0.0125 atm and 0.0375 atm respectively, at a total pressure of 1.25 atm. From the *in situ* measurements we find that at these temperatures FeNC is primarily composed of metallic Fe, and Fe₃C, and Fe₃C was reported as a weakly active catalyst for methanol synthesis from CO₂ [80]. Cu doping improved the performance of FeNC, at first by promoting its reduction to a mixture of metallic Fe and Fe₃C at lower temperatures and at the second by the offering of active sites for adsorption of hydrogen during reaction course.

Overall, the performance of the Cu-FeNC catalyst at low pressure positions this catalysts among the best reported catalyst for CO₂ conversion. The obtained activation energies (E_a) shown in Table 1 are lower in comparison with reported values for bulk catalysts [6,76]. The activation energies are comparable with those obtained for sub-nanometer sized Cu clusters and extended Cu surfaces [13,14]. The anti-correlation of the evolution of the methanol, CO and methane formation on the Cu-FeNC catalysts is in accord with earlier reports [13,14].

3.3.3. Benzene formation

Benzene was also formed with FeNC catalyst as shown in Fig. 7c, at TORs up to 1.5×10^{-7} molecules atom $^{-1}$ s $^{-1}$ (0.3 g kg $^{-1}$ h $^{-1}$). The TOR drops to 0.5×10^{-7} molecules atom $^{-1}$ s $^{-1}$ (0.1 g kg $^{-1}$ h $^{-1}$) with Cu-FeNC catalyst, as another demonstration of the effect of copper on the activity and selectivity of the catalyst. Low TOR towards benzene for Cu-FeNC at 375 °C could be due to the significant increase in selectivity towards methane and CO through efficient hydrogen splitting, at the expense of benzene formation. We also hypothesize that Cu may block some of the active sites where benzene formation takes place.

In the case of Cu-FeNC and FeNC about 60% and 40% of the converted CO₂ goes towards formation of CO, methane, methanol, benzene, respectively. The remaining CO₂ can be consumed by the formation of other products not monitored in the experiment and by the formation of iron carbide [15]. Possible products may include longer

chain hydrocarbons (see, e.g. REF [72]). For example we have detected additional mass spectrometer signals at 56 m/z and 54 m/z, which could have their origin for example in cyclohexane and cyclohexene respectively. However, these masses can be fragments from variety of substances, so without firm evidence we prefer not to speculate. The total carbon pickup by the catalyst is estimated to be around 0.125 mg for both Cu-FeNC and FeNC samples. The Fe content in the catalyst has been determined by ICP-MS and the fraction of the iron carbide obtained is obtained from XANES. An estimate based on CO₂ TOR of 0.005 molecules/atom/s at 375 °C, we find that in 30 min (which is the residual time at 375 °C, when all the carbides are forming), the total conversion for the carbon portion of CO₂ is 1.9 mg in one single step. This implies one out of 15 carbon atoms converted from CO₂ goes towards carburization. The rest are converted to CO, methane, methanol, benzene, and the other longer chain products like cyclohexane and cyclohexene. Water has also been detected in the MID during the reaction and is shown in Fig. S8.

Here we attempt to provide an insight on the role of a specific composition within the working catalyst for the products formed, though an unambiguous assignment is challenging due to the changing catalyst composition with temperature change during the ramp. Presence of minor amount of Fe₅C₂ in the working catalyst was reported based on XRD analysis which can be responsible for methanol formation based on a recent study [72]. Fe⁰ and Fe₃C, which is the abundant composition drives the reaction more favourable towards methane and benzene [72,80]. Cu plays a bifunctional role acting as a promoter in activating/splitting hydrogen, which also enhances the reduction of the catalyst and its overall activity. The significantly higher methanol production at 225 and 275 °C on the Cu-FeNC catalyst provides evidence that Cu also serves as an additional active site, in accord with reports on methanol formation by Cu alone.

4. Conclusion

We synthesized two types of iron oxide based nanocatalysts prepared by sonication methods, namely iron oxide blank (FeNC) and iron oxide decorated with copper nanoparticles (Cu-FeNC). To obtain highly dispersed Cu, for Cu-FeNC we applied a new synthesis route where in the second step of synthesis copper was added to the pre-made iron oxide by sonication with a Cu salt in the presence of a moderately strong reducing agent. *In situ* X-ray scattering reveals the initial restructuring of the catalyst at the nanometer scale. An *in situ* X-ray absorption characterization of the catalysts performed under reaction conditions showed that the initial iron oxide and oxyhydroxide components of the catalyst reduces to a mixture of metallic iron and iron carbide, and the presence of copper accelerates this transformation as copper reduces. Microscopies, Raman and X-ray diffraction provided complementary information for the interpretation of the *in situ* data and for a better understanding of the evolution of the structure, morphology and composition of the catalysts. The Cu-FeNC catalysts were found efficient to convert CO₂ at a low partial pressure of CO₂ and H₂ (0.0125 atm and 0.0375 atm). Per total Fe atom turnover rates of up to 3×10^{-3} , 1.5×10^{-3} , 5.4×10^{-4} , and 4×10^{-6} molecules atom $^{-1}$ s $^{-1}$ for CO, methane, methanol, and benzene, respectively are obtained, moreover at low activation energies.

This work suggests a perspective direction to produce efficient catalyst for low-pressure conversion of CO₂.

Acknowledgement

The authors from RCPTM gratefully acknowledge support from the Ministry of Education, Youth and Sports of the Czech Republic by the projects LO1305 and LM2015073.

Table 1

Activation energies (in kJ mol $^{-1}$) of reaction products for FeNC and Cu-FeNC catalysts.

	CO (m/ z = 28)	Methane (m/ z = 15)	Methanol (m/ z = 31)	Benzene (m/ z = 78)
FeNC	45	40	37	60
Cu-FeNC	46	45	32	39

Appendix A. Supplementary data

Supplementary data associated with this article can be found, in the online version, at <https://doi.org/10.1016/j.apcatb.2017.11.047>.

References

- [1] R. Satthawong, N. Koizumi, C.S. Song, P. Prasassarakich, Comparative study on CO_2 hydrogenation to higher hydrocarbons over Fe-based bimetallic catalysts, *Top. Catal.* 57 (2014) 588–594.
- [2] X.M. Liu, G.Q. Lu, Z.F. Yan, J. Beltramini, Recent advances in catalysts for methanol synthesis via hydrogenation of CO and CO_2 , *Ind. Eng. Chem. Res.* 42 (2003) 6518–6530.
- [3] G.A. Olah, A. Goeppert, G.K.S. Prakash, Chemical recycling off carbon dioxide to methanol and dimethyl ether: from greenhouse gas to renewable, environmentally carbon neutral fuels and synthetic hydrocarbons, *J. Org. Chem.* 74 (2009) 487–498.
- [4] M.R. Rahimpour, K. Alizadehhesari, Enhancement of carbon dioxide removal in a hydrogen-permselective methanol synthesis reactor, *Int. J. Hydro. Energy* 34 (2009) 1349–1362.
- [5] W.J. Cai, P.R. de la Piscina, J. Toyir, N. Homs, CO_2 hydrogenation to methanol over Cu/ZnGa catalysts prepared using microwave-assisted methods, *Catal. Today* 242 (2015) 193–199.
- [6] W. Wei, G. Jinlong, Methanation of carbon dioxide: an overview, *Front. Chem. Sci. Eng.* 5 (2011) 2–10.
- [7] G. Bozzano, F. Manenti, Efficient methanol synthesis: perspectives, technologies and optimization strategies, *Prog. Energy Combust.* 56 (2016) 71–105.
- [8] H. Ahouari, A. Soualah, A. Le Valant, L. Pinard, P. Magnoux, Y. Pouilloux, Methanol synthesis from CO_2 hydrogenation over copper based catalysts, *React. Kinet. Mech. Catal.* 110 (2013) 131–145.
- [9] A. Baiker, Utilization of carbon dioxide in heterogeneous catalytic synthesis, *Appl. Organomet. Chem.* 14 (2000) 751–762.
- [10] H. Sakurai, M. Haruta, Carbon-dioxide and carbon-monoxide hydrogenation over gold supported on titanium, iron, and zinc-oxides, *Appl. Catal. a-Gen.* 127 (1995) 93–105.
- [11] R. Sahki, O. Benlounes, O. Cherifi, R. Thouvenot, M.M. Bettahar, S. Hocine, Effect of pressure on the mechanisms of the CO_2/H_2 reaction on a CO-precipitated $\text{CuO}/\text{ZnO}/\text{Al}_2\text{O}_3$ catalyst, *React. Kinet. Mech. Catal.* 103 (2011) 391–403.
- [12] G.C. Chinchen, P.J. Denny, D.G. Parker, M.S. Spencer, D.A. Whan, Mechanism of methanol synthesis from $\text{CO}_2/\text{CO}/\text{H}_2$ mixtures over copper/zinc oxide/alumina catalysts – use of C-14-labeled reactants, *Appl. Catal.* 30 (1987) 333–338.
- [13] C. Liu, B. Yang, E. Tyo, S. Seifert, J. DeBartolo, B. von Issendorff, P. Zapol, S. Vajda, L.A. Curtiss, Carbon dioxide conversion to methanol over size-selected Cu_4 clusters at low pressures, *J. Am. Chem. Soc.* 137 (2015) 8676–8679.
- [14] B. Yang, C. Liu, A. Halder, E.C. Tyo, A.B.F. Martinson, S. Seifert, P. Zapol, L.A. Curtiss, S. Vajda, Copper cluster size effect in methanol synthesis from CO_2 , *J. Phys. Chem. C* (2017).
- [15] J. Kirchner, J.K. Anolleck, H. Lösch, S. Kureti, Methanation of CO_2 on iron based catalysts, *Appl. Catal. B Environ.* (2017).
- [16] S.H. Kang, J.W. Bae, P.S.S. Prasad, J.H. Oh, K.W. Jun, S.L. Song, K.S. Min, Influence of Ga addition on the methanol synthesis activity of Cu/ZnO catalyst in the presence and absence of alumina, *J. Ind. Eng. Chem.* 15 (2009) 665–669.
- [17] M. Muhler, E. Tornqvist, L.P. Nielsen, B.S. Clausen, H. Topsøe, On the role of adsorbed atomic oxygen and CO_2 in copper-based methanol synthesis catalysts, *Catal. Lett.* 25 (1994) 1–10.
- [18] Y. Yang, C.A. Mims, D.H. Mei, C.H.F. Peden, C.T. Campbell, Mechanistic studies of methanol synthesis over Cu from $\text{CO}/\text{CO}_2/\text{H}_2/\text{H}_2\text{O}$ mixtures: the source of C in methanol and the role of water, *J. Catal.* 298 (2013) 10–17.
- [19] M.D. Lee, J.F. Lee, C.S. Chang, T.Y. Dong, Effects of addition of chromium manganese, or molybdenum to iron catalysts for carbon-dioxide hydrogenation, *Appl. Catal.* 72 (1991) 267–281.
- [20] L.K. Obid Tursunov, Aleksander Kustov, Andrey Travyanov, A brief review of CO_2 hydrogenation to methanol over Cu- and Fe-based catalysts, Proceedings of 48th IASTEM International Conference, New York, USA, 15th–16th March, 2017, pp. 1–8.
- [21] P.H. Choi, K.W. Jun, S.J. Lee, M.J. Choi, K.W. Lee, Hydrogenation of carbon dioxide over alumina supported Fe-K catalysts, *Catal. Lett.* 40 (1996) 115–118.
- [22] L.M. Chew, H. Ruland, H.J. Schulte, W. Xia, M. Muhler, CO_2 hydrogenation to hydrocarbons over iron nanoparticles supported on oxygen-functionalized carbon nanotubes, *J. Chem. Sci.* 126 (2014) 481–486.
- [23] K.S. Lin, A.K. Adhikari, K. Dehvari, J.H. Yang, C.W. Shu, Fine structural characterization of zinc and iron atoms in zinc ferrite nanocatalysts for CO_2 decomposition using XANES/EXAFS, *Chinese J. Phys.* 50 (2012) 271–282.
- [24] S.S. Nam, H. Kim, G. Kishan, M.J. Choi, K.W. Lee, Catalytic conversion of carbon dioxide into hydrocarbons over iron supported on alkali ion-exchanged Y-zeolite catalysts, *Appl. Catal. a-Gen.* 179 (1999) 155–163.
- [25] Z.H. Suo, Y. Kou, J.Z. Niu, W.Z. Zhang, H.L. Wang, Characterization of TiO_2 , ZrO_2 and Al_2O_3 -supported iron catalysts as used for CO_2 hydrogenation, *Appl. Catal. a-Gen.* 148 (1997) 301–313.
- [26] Y. Kou, Z.H. Suo, J.Z. Niu, W.Z. Zhang, H.L. Wang, Surface coordinate geometry of iron catalysts – hydrogenation of CO_2 over Fe/ZrO_2 prepared by a novel method, *Catal. Lett.* 35 (1995) 271–277.
- [27] G. Ertl, H. Knözinger, J. Weitkamp, *Handbook of Heterogeneous Catalysis*, VCH, Weinheim, 1997.
- [28] P. Courty, H. Ajot, C. Marcilly, B. Delmon, Oxides, mixed or in solid-solution, highly dispersed obtained by thermal decomposition of amorphous precursors, *Powder Technol.* 7 (1973) 21–38.
- [29] T. Inui, K. Kitagawa, T. Takeguchi, T. Hagiwara, Y. Makino, Hydrogenation of carbon dioxide to C1–C7 hydrocarbons via methanol on composite catalysts, *Appl. Catal. a-Gen.* 94 (1993) 31–44.
- [30] S. Natesakawat, J.W. Lekse, J.P. Baltrus, P.R. Ohodnicki, B.H. Howard, X.Y. Deng, C. Matranga, Active sites and structure-activity relationships of copper-based catalysts for carbon dioxide hydrogenation to methanol, *ACS Catal.* 2 (2012) 1667–1676.
- [31] G.G. Wang, Y.Z. Zuo, M.H. Han, J.F. Wang, Copper crystallite size and methanol synthesis catalytic property of Cu-based catalysts promoted by Al, Zr and Mn, *React. Kinet. Mech. Catal.* 101 (2010) 443–454.
- [32] D.J. Wang, F.R. Tao, H.H. Zhao, H.L. Song, L.J. Chou, Preparation of $\text{Cu}/\text{ZnO}/\text{Al}_2\text{O}_3$ catalyst for CO_2 hydrogenation to methanol by CO_2 assisted aging, *Chinese J. Catal.* 32 (2011) 1452–1456.
- [33] A. Bansode, A. Urakawa, Towards full one-pass conversion of carbon dioxide to methanol and methanol-derived products, *J. Catal.* 309 (2014) 66–70.
- [34] M. Sahibzada, D. Chadwick, I.S. Metcalfe, Hydrogenation of carbon dioxide to methanol over palladium-promoted $\text{Cu}/\text{ZnO}/\text{Al}_2\text{O}_3$ catalysts, *Catal. Today* 29 (1996) 367–372.
- [35] M. Sahibzada, I.S. Metcalfe, D. Chadwick, Methanol synthesis from $\text{CO}/\text{CO}_2/\text{H}_2$ over $\text{Cu}/\text{ZnO}/\text{Al}_2\text{O}_3$ at differential and finite conversions, *J. Catal.* 174 (1998) 111–118.
- [36] C.S. Song, Global challenges and strategies for control conversion and utilization of CO_2 for sustainable development involving energy, catalysis, adsorption and chemical processing, *Catal. Today* 115 (2006) 2–32.
- [37] H. Mistry, F. Behafarid, R. Reske, A.S. Varela, P. Strasser, B. Roldan Cuenya, Tuning catalytic selectivity at the mesoscale via interparticle interactions, *ACS Catal.* 6 (2016) 1075–1080.
- [38] R. Reske, H. Mistry, F. Behafarid, B. Roldan Cuenya, P. Strasser, Particle size effects in the catalytic electroreduction of CO_2 on Cu nanoparticles, *J. Am. Chem. Soc.* 136 (2014) 6978–6986.
- [39] R.V. Kumar, Y. Mastai, Y. Diamant, A. Gedanken, Sonochemical synthesis of amorphous Cu and nanocrystalline Cu_2O embedded in a polyaniline matrix, *J. Mater. Chem.* 11 (2001) 1209–1213.
- [40] N. Perkas, G. Amirian, C. Rottman, F. de la Vega, A. Gedanken, Sonochemical deposition of magnetite on silver nanocrystals, *Ultrason. Sonochem.* 16 (2009) 132–135.
- [41] R. Zboril, L. Machala, M. Mashlan, M. Hermanek, M. Miglierini, A. Fojtik, Structural, magnetic and size transformations induced by isothermal treatment of ferrous oxalate dihydrate in static air conditions, Second Seeheim Conference on magnetism, *Proceedings* (2004) 3583–3588.
- [42] K.J. Datta, M.B. Gawande, K.K.R. Datta, V. Ranc, J. Pechousek, M. Krizek, J. Tucek, R. Kale, P. Pospisil, R.S. Varma, T. Asefa, G. Zoppellaro, R. Zboril, Micro-mesoporous iron oxides with record efficiency for the decomposition of hydrogen peroxide: morphology driven catalysis for the degradation of organic contaminants, *J. Mater. Chem. A* 4 (2016) 596–604.
- [43] S. Vajda, S. Lee, K. Sell, I. Barke, A. Kleibert, V. von Oeynhausen, K.H. Meiwes-Broer, A.F. Rodriguez, J.W. Elam, M.M. Pellin, B. Lee, S. Seifert, R.E. Winans, Combined temperature-programmed reaction and in situ X-ray scattering studies of size-selected silver clusters under realistic reaction conditions in the epoxidation of propene, *J. Chem. Phys.* 131 (2009).
- [44] E.C. Tyo, C.R. Yin, M. Di Vece, Q. Qian, G. Kwon, S. Lee, B. Lee, J.E. DeBartolo, S. Seifert, R.E. Winans, R. Si, B. Ricks, S. Goergen, M. Rutter, B. Zugic, M. Flytzani-Stephanopoulos, Z.W. Wang, R.E. Palmer, M. Neurock, S. Vajda, Oxidative dehydrogenation of cyclohexane on cobalt oxide (Co_3O_4) nanoparticles: the effect of particle size on activity and selectivity, *ACS Catal.* 2 (2012) 2409–2423.
- [45] J.A. Wang, R.E. Winans, S.L. Anderson, S. Seifert, B. Lee, P.J. Chupas, Y. Ren, S. Lee, Y.Z. Liu, In situ small-angle X-ray scattering from Pd nanoparticles formed by thermal decomposition of organo-Pd catalyst precursors dissolved in hydrocarbons, *J. Phys. Chem. C* 117 (2013) 22627–22635.
- [46] S. Lee, B. Lee, S. Seifert, S. Vajda, R.E. Winans, Simultaneous measurement of X-ray small angle scattering, absorption and reactivity: a continuous flow catalysis reactor, *Nucl. Instrum. Methods A* 649 (2011) 200–203.
- [47] P. Moore, Small-angle scattering. Information content and error analysis, *J. Appl. Crystalllogr.* 13 (1980) 168–175.
- [48] B. Ravel, M. Newville, ATHENA, ARTEMIS, HEPHAESTUS: data analysis for X-ray absorption spectroscopy using IFEFFIT, *J. Synchrotron Radiat.* 12 (2005) 537–541.
- [49] R. Passalacqua, S. Parathoner, G. Centi, A. Halder, E.C. Tyo, B. Yang, S. Seifert, S. Vajda, Electrochemical behaviour of naked sub-nanometre sized copper clusters and effect of CO_2 , *Catal. Sci. Technol.* 6 (2016) 6977–6985.
- [50] J. Sanchez-Marcos, M.A. Laguna-Marcos, R. Martinez-Morillas, E. Cespedes, F. Jimenez-Villacorta, N. Menendez, C. Prieto, Exchange bias in iron oxide nanoclusters, *J. Phys.-Condens. Matter* 23 (2011).
- [51] A.N. Maratkanova, A.V. Syugaev, D.A. Petrov, S.F. Lomayeva, Structural characterization and microwave properties of chemically functionalized iron particles obtained by high-energy ball milling in paraffin-containing organic environment, *Powder Technol.* 274 (2015) 349–361.
- [52] W. Karim, C. Spreafico, A. Kleibert, J. Gobrecht, J. Vandevondele, Y. Ekinici, J.A. van Bokhoven, Catalyst support effects on hydrogen spillover, *Nature* 541 (2017) 68–71.
- [53] R. Burch, S.E. Golunski, M.S. Spencer, The role of hydrogen in methanol synthesis over copper catalysts, *Catal. Lett.* 5 (1990) 55–60.
- [54] M. Bani-Hani, R. Abd-Allah, L. El-Khoury, Archeometallurgical finds from Barsinia, Northern Jordan: microstructural characterization and conservation treatment, *J. Cult. Herit.* 13 (2012) 314–325.

- [55] M.A. Irfan, D. Schwam, A. Karve, R. Ryder, Porosity reduction and mechanical properties improvement in die cast engine blocks, *Mater. Sci. Eng.: A* 535 (2012) 108–114.
- [56] F.N. Sayed, V. Polshettiwar, Facile and sustainable synthesis of shaped iron oxide nanoparticles: effect of iron precursor salts on the shapes of iron oxides, *Sci. Rep.* 5 (2015) 9733.
- [57] G. Khayatian, S. Hassanpoor, A.R.J. Azar, S. Mohebbi, Spectrophotometric determination of trace amounts of uranium(VI) using modified magnetic iron oxide nanoparticles in environmental and biological samples, *J. Braz. Chem. Soc.* 24 (2013) 1808–1817.
- [58] M.B. Zakaria, Nanostructuring of nanoporous iron carbide spheres via thermal degradation of triple-shelled Prussian blue hollow spheres for oxygen reduction reaction, *RSC Adv.* 6 (2016) 10341–10351.
- [59] D. Wagner, O. Devisme, F. Patisson, D. Ablitzer, A laboratory study of the reduction of iron oxides by hydrogen, in: F.R. Kongoli, R.G. Reddy (Eds.), *Sohn International Symposium Advanced Processing of Metals and Materials, Minerals, Metals & Materials Soc, USA Aug 27–31, 2006*, pp. 111–120.
- [60] F.G. Javier A. Lopez, Flavio A. Bonilla, Gustavo Zambrano, Maria E. Gómez, Synthesis and characterization of Fe_3O_4 magnetic nanofluid, *Revista Latinoamericana de Metalurgia y Materiales* 30 (2010) 60–66.
- [61] I.S. Molchan, G.E. Thompson, R. Lindsay, P. Skeldon, V. Likodimos, G.E. Romanos, P. Falaras, G. Adamova, B. Iliev, T.J.S. Schubert, Corrosion behaviour of mild steel in 1-alkyl-3-methylimidazolium tricyanomethanide ionic liquids for CO_2 capture applications, *RSC Adv.* 4 (2014) 5300–5311.
- [62] I. Chourpa, L. Douziech-Eyrrolles, L. Ngaboni-Okassa, J.F. Fouquenet, S. Cohen-Jonathan, M. Souce, H. Marchais, P. Dubois, Molecular composition of iron oxide nanoparticles precursors for magnetic drug targeting, as characterized by confocal Raman microspectroscopy, *Analyst* 130 (2005) 1395–1403.
- [63] M. Hanesch, Raman spectroscopy of iron oxides and (oxy)hydroxides at low laser power and possible applications in environmental magnetic studies, *Geophys. J. Int.* 177 (2009) 941–948.
- [64] F.F. Gao, H. Wang, M. Qing, Y. Yang, Y.W. Li, Controlling the phase transformations and performance of iron-based catalysts in the Fischer-Tropsch synthesis, *Chinese J. Catal.* 34 (2013) 1312–1325.
- [65] X. Zhang, Y. Niu, X. Meng, Y. Li, J. Zhao, Structural evolution and characteristics of the phase transformations between [small alpha]- Fe_2O_3 , Fe_3O_4 and [gamma]- Fe_2O_3 nanoparticles under reducing and oxidizing atmospheres, *CrystEngComm* 15 (2013) 8166–8172.
- [66] L. Wang, X. Lu, C. Han, R. Lu, S. Yang, X. Song, Electrosprayed hollow cage-like [small alpha]- Fe_2O_3 microspheres: synthesis, formation mechanism, and morphology-preserved conversion to Fe nanostructures, *CrystEngComm* 16 (2014) 10618–10623.
- [67] D.L.A. de Faria, S. Venâncio Silva, M.T. de Oliveira, Raman microspectroscopy of some iron oxides and oxyhydroxides, *J. Raman Spectrosc.* 28 (1997) 873–878.
- [68] K. Murugappan, D.S. Silvester, D. Chaudhary, D.W.M. Arrigan, Electrochemical characterization of an oleyl-coated magnetite nanoparticle-modified electrode, *ChemElectroChem* 1 (2014) 1211–1218.
- [69] P. Zhang, X. Wang, W. Wang, X. Lei, H. Yang, Iron carbide and nitride via a flexible route: synthesis, structure and magnetic properties, *RSC Adv.* 5 (2015) 21670–21674.
- [70] T.K. Townsend, E.M. Sabio, N.D. Browning, F.E. Osterloh, Photocatalytic water oxidation with suspended alpha- Fe_2O_3 particles-effects of nanoscaling, *Energy Environ. Sci.* 4 (2011) 4270–4275.
- [71] R. Prakash, A.K. Mishra, A. Roth, C. Kubel, T. Scherer, M. Ghafari, H. Hahn, M. Fichtner, A ferrocene-based carbon-iron lithium fluoride nanocomposite as a stable electrode material in lithium batteries, *J. Mater. Chem.* 20 (2010) 1871–1876.
- [72] J. Wei, Q. Ge, R. Yao, Z. Wen, C. Fang, L. Guo, H. Xu, J. Sun, Directly converting CO_2 into a gasoline fuel, *Nat. Commun.* 8 (2017) 15174.
- [73] S. Elzey, J. Baltrusaitis, S. Bian, V.H. Grassian, Formation of paratacamite nanomaterials via the conversion of aged and oxidized copper nanoparticles in hydrochloric acidic media, *J. Mater. Chem.* 21 (2011) 3162–3169.
- [74] H. Wang, J. Hodgson, T.B. Shrestha, P.S. Thapa, D. Moore, X. Wu, M. Ikenberry, D.L. Troyer, D. Wang, K.L. Hohn, S.H. Bossmann, Carbon dioxide hydrogenation to aromatic hydrocarbons by using an iron/iron oxide nanocatalyst, *Beilstein J. Nanotechnol.* 5 (2014) 760–769.
- [75] M. Albrecht, U. Rodemerck, M. Schneider, M. Bröring, D. Baabe, E.V. Kondratenko, Unexpectedly efficient CO_2 hydrogenation to higher hydrocarbons over non-doped Fe_2O_3 , *Appl. Catal. B: Environ.* 204 (2017) 119–126.
- [76] J. Yoshihara, S.C. Parker, A. Schafer, C.T. Campbell, Methanol synthesis and reverse water-gas shift kinetics over clean polycrystalline copper, *Catal. Lett.* 31 (1995) 313–324.
- [77] S. Lee, B. Lee, S. Seifert, R.E. Winans, S. Vajda, Fischer-Tropsch synthesis at a low pressure on subnanometer cobalt oxide clusters: the effect of cluster size and support on activity and selectivity, *J. Phys. Chem. C* 119 (2015) 11210–11216.
- [78] L. Schimka, J. Harl, A. Stroppa, A. Grüneis, M. Marsman, F. Mittendorfer, G. Kresse, Accurate surface and adsorption energies from many-body perturbation theory, *Nat. Mater.* 9 (2010) 741–744.
- [79] A.K. Srivastava, A. Saxena, D. Shah, T.H. Mahato, B. Singh, A.R. Shrivastava, P.K. Gutch, C.P. Shinde, Catalytic removal of carbon monoxide over carbon supported palladium catalyst, *J. Hazard. Mater.* 241 (2012) 463–471.
- [80] J.L. Dubois, K. Sayama, H. Arakawa, CO_2 hydrogenation over carbide catalysts, *Chem. Lett.* (1992) 5–8.